Effect of polarization in evanescent wave amplification for the enhancement of scattering of nanoparticles on surfaces

Kolenov, Dmytro; Urbach, Paul; Pereira, Silvania

DOI
10.1364/OSAC.385908

Publication date
2020

Document Version
Final published version

Published in
OSA Continuum

Research Article Vol. 3, No. 4 / 15 April 2020 / OSA Continuum 742

Effect of polarization in evanescent wave amplification for the enhancement of scattering of nanoparticles on surfaces

D. KOLENOV,* H. P. URBACH, AND S. F. PEREIRA

Optics Research Group, Imaging Physics Department, Faculty of Applied Sciences, Delft University of Technology, Lorentzweg 1, 2628 CJ Delft, The Netherlands
d.kolenov@tudelft.nl

Abstract: We demonstrate the far field detection of low-contrast nanoparticles on surfaces using a technique that is based on evanescent-wave amplification due to a thin dielectric layer that is deposited on the substrate. This research builds upon earlier results where scattering enhancement of 200 nm polystyrene (PSL) particles on top of a glass substrate covered with a ≈ 20 nm InSb layer has been observed by Roy *et al*. [Phys. Rev. A **96**, 013814 (2017)]. In this paper, the enhancement effect is analyzed using other dielectric materials with lower absorption than the previous one, resulting in a higher signal-to-noise ratio (SNR) for particle detection. We also consider several polarizations of the incoming field, such as linear, circular, azimuthal, and radial. In our experiments, we observe that the optimum enhancement occurs when linear polarization is used. With this new scheme, PSL nanoparticles of 40 nm in diameter have been detected at a wavelength of 405 nm.

1. Introduction

The need for the detection and size identification of (bio-) nanoparticles has been one of the main driving forces for a number of the near-field and far-field optical techniques in the last few decades. In turn, single molecule detection is one of the fundamental challenges of modern biology [1]. The behaviour of individual particles and molecules can have significant implications in both properties of individual cells and biochemical processes [2]. Notably, bio-nanoparticles such as exosomes or viruses are known to be important bio-markers for a range of medical experiments [3]. They are challenging to visualize via optical means because they are index-matched with the substrate [4]. Additionally, their size is small such as viruses range from 18 to 300 nm and exosomes from 30 to 100 nm in diameter [5]. When imaging nanoparticles with sizes $< \lambda/8$ in diameter, the diffraction limit of optical systems becomes a limiting factor [6]. Existing labeling techniques found in fluorescence microscopy can overcome the diffraction limit. For example, wide-field epi-illumination confocal microscopy combined with fluorescence are popular methods for single particle detection. A review of these methods can be found in Ref. [5]. However, such techniques have a drawback due to the complexity of sample preparation and labeling [3]. Another popular approach is near field optical microscopy (NSOM). Nevertheless, it also has drawbacks because of tip perturbations, risk to add contamination to the sample, and limited throughput [5].

In the last few years, new detection schemes have been introduced that eliminate the need of fluorophores and work in the far field. For instance, the technique called common path wide-field interferometric microscopy [6], that uses a layered substrate. It works in reflection mode, and the function of the extra layer is to eliminate the background due to destructive interference. The strength of this technique is that the detection is at the far-field and is very sensitive to subwavelength nanoparticles with small optical contrast [7].

#385908 https://doi.org/10.1364/OSAC.385908
Journal © 2020 Received 19 Dec 2019; revised 2 Mar 2020; accepted 2 Mar 2020; published 17 Mar 2020

OSA CONTINUUM

The use of layers on the substrate as extra "tool" allow subwavelength detection of single particles is also the heart of the technique that is discussed in this paper, but the principle is quite different than common path interference microscopy. Essentially, our method is based on exploring the interaction between the incoming light with the nanoparticle and the substrate with the latter having a thin layer of dielectric material deposited on it. This interaction results in evanescent wave amplification in the near field and enhancement of the scattering to the far field [8,9]. Here, we go one step forward with this method by presenting a study on appropriate materials (dielectric) and thickness for the thin layer and an analysis on the influence of the polarization state of the input light. We show that by optimizing the system, one can drastically improve the sensitivity of the detection of nanoparticles. Further, we demonstrate detection of 40 nm PSL nanoparticles in diameter with a wavelength of 405 nm.

The remainder of the paper is organized as follows: Section 2.1 is devoted to the description of the optical system, and in Section 2.2 the mechanism behind the amplification is discussed. In Section 3, we present the overview of materials that are suitable for evanescent wave amplification. Section 4 shows the rigorous simulations of the scattering system. In Section 5, we present the experimental results, and, in Section 6 and 7, we finalize the paper with discussions and conclusions, respectively.

2. Methods

The optical system we analyze in this paper is similar to a confocal microscope operating in reflection mode. The illumination of the sample is a laser beam that is focused by a high numerical aperture microscope objective. The far field signal is obtained by scanning the sample in the lateral direction, and for each scanning position, the reflected light is detected by a photodetector. One major difference of our system as compared to confocal microscopes is that we do not detect the image plane at the detector, but the image of the back focal plane of the objective. Thus, at the detector plane, the full scattered field within the numerical aperture of the system is detected. This far field is a 2D light distribution where each pixel corresponds to one scattered angle. Since the system is coherent, it means that for each scattered angle, the signal corresponds to the interference between the scattered light by the object and the substrate. Although the full scattered field contains a lot of information regarding the particle, we have seen that enough information about the position and size of particle can be obtained by simply dividing the far field in two halves (perpendicular to the scan direction), integrating both halves using a split detector and subtracting them. In this way, only one photocurrent value is recorded for each scanning position.

2.1. Experimental scheme

The experimental setup is shown in Fig. 1(A). The light source is a blue diode laser (405 nm by Power Technology, model: IQ1A25) that is polarized before it approaches the focusing lens of numerical aperture $NA = 0.9$ (OBJ in the figure). The objective is a non commercial objective designed for mastering CDs in optical data storage. The focused spot is $\approx 1\ \mu m$. The high numerical aperture allows for the collection of a large number of diffracted angles within the illumination cone of the light. These include the scattered and reflected fields from the nanoparticle and substrate. The state of the polarization is crucial because the shape and size of the spot that is formed in the plane of the particle will vary as well as the 3D polarization distribution of the field in focus. A telescopic arrangement formed by LENS2 and LENS3 is used to fit the reflected beam into the area of the split detector (SD). Recorded signals from the photodetector are the basis for the signal maps. In our system, SD is bi-cell silicon photodiode from Advanced Photonix. The sample is mounted on a 3D piezo-electric stage whose position can be controlled with sub-nm precision (P-629.2CD by Physik Instrumente.)

OSA CONTINUUM

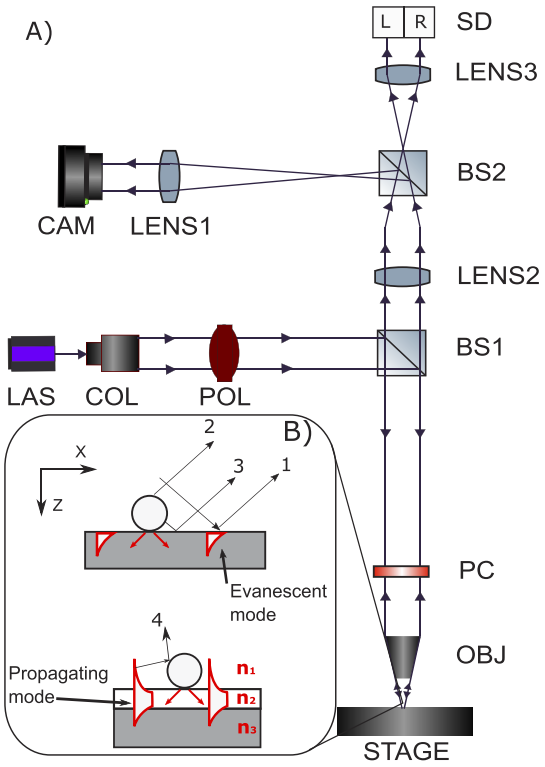

Fig. 1. A sketch of the experimental setup: A) (STAGE: piezo-electric XYZ translator; OBJ: objective lens; PC: polarizator convertor (zero-order vortex half-wave retarder); BS1, BS2: beam splitters; POL: linear polarizer, COL: light collimator, LENS1, LENS2, LENS3 converging lenses; CAM: CCD camera used for localizing the sample; SD: split detector (bi-cell silicon photodiode), LAS: blue diode laser. B) Top: the scattered and reflected components that contribute to the far field signal and evanescent modes decay quickly in the substrate and in air. Bottom: evanescent waves at the interface due to the presence of a thin layer on the substrate are amplified and re-scattered by the particle.

In order to generate azimuthal or radial polarization, we add a liquid crystal polarizator convertor (PC in the figure, zero-order vortex half wave retarder from Thorlabs) before the objective (OBJ), otherwise the polarization is linear. The camera (CAM) is used for localizing the sample.

Note that our scheme operates in bright field and not in dark field as it is the case of some nanoparticle detectors based on far field scattering [10].

2.2. *Enhancement mechanism*

The light at the split detector is a superposition of mainly three contributions (see Fig. 1(B) top): the mirror-like reflected field from the substrate (1), the direct scattered field by the particle (2), the field scattered by the particle that is further reflected from the substrate (3). The scattering from the particle on top of substrate can generate the weak evanescent mode that decays very fast and cannot reach the detector. When switching to, e.g. the 3-layer system (air, enhancement layer, substrate with refractive indices n_1, n_2 and n_3), a fourth channel (4) can be invoked; firstly, the particle couples light to the modes that can propagate in the layer (Fig. 1(B) bottom), hence it is critical that $n_2 > n_1$ and $n_2 > n_3$, and secondly, the generated decaying tail is converted

OSA CONTINUUM

to the propagating modes by re-scattering from particle [8,9]. It is crucial to create such an enhancement layer that the amount of the decay towards the first medium is maximum.

We believe that the evanescent wave amplification that we employ is highly relevant for biological applications because it manifests itself even with low power illumination such as in the range of smaller than 1 mW, as we will show experimentally. Low illumination power is important in systems where the specimen could be damaged through heat [11]. Our approach is more efficient than only using the massive power of illumination for one more reason: in the proposed mechanism, we can amplify a characteristic signal from particle rather than from its surroundings. To overcome the noise level, we introduce and tune the thickness and material of the enhancement layer until it has a sizable contribution on the evanescent field, and this light is being re-scattered specifically by a sphere.

3. Thin film material analysis

One should choose a suitable material to achieve enhanced scattering. Firstly, for the probing wavelength of interest, the layer should have both a higher refractive index than the substrate surface $n_2 > n_3$ and low absorption to allow the guiding. Secondly, in applications in which the transmission properties of the resulting stack should be high, the enhancement layer should be very thin (of the order of a few tens of nanometers) in order to avoid much light loss because of absorption. Finally, the thickness should be tuned so that the most substantial evanescent part of the spectra builds up near the interface between the host medium n_1 (e.g. air) and top layer n_2.

Enhancing the far-field response by coating the glass or plastic substrate with a single layer of dielectric is convenient because, in the visible regime, it is relatively straightforward to find materials that do have a higher refractive index than glass or plastic. See, for example, the set of common dielectric and semiconductor materials shown in Table 1.

Table 1. Examples of dielectric and semiconductor materials that can act as single layer evanescent wave amplification. The optical properties are defined for the wavelength 405 nm. The substrate should have a lower refractive index than a cover layer to allow the guiding. Deposition processes are Evaporation: conventional thermal evaporation in high vacuum, EPVD: Electron-beam physical vapor deposition, CVD: chemical vapor deposition techniques, Arc-PVD: cathodic arc plasma deposition. Ext. coeff. refers to extinction coefficient.

Material	Index	Ext. coeff.	Process
TiO_2	2.5	1e-10/≈ zero	Evaporation + Arc-PVD
Ta_2O_5	2.15	1e-4	EPVD
Si_3N_4	2.09	≈ zero	CVD
c-Si	4.4 or 5.437	2.3 or 0.34	CVD
GaP	4.15	0.25	CVD
Ge	4.11	2.18	Evaporation
InSb	3.39	2	CVD
alpha-Si	3.8	2.5 or 0.5 process dependent	EPVD

Our goal is to maximize the scattering that reaches the detector. In the case of very small particles, it is crucial that the surface under the particle is smooth and does not introduce too much scattering. Dielectric materials are favored because they allow large area and homogeneous deposition with high levels of smoothness.

In addition, one should add that the enhancement mechanism considered here is different compared to conventional ways of getting greater optical response from the surface under

OSA CONTINUUM

inspection such as high reflecting surfaces by introducing metal or by producing sandwich-structured layers. By using one single dielectric layer, our approach offers the elegance regarding both simplicity and surface uniformity. The selection of the dielectric materials which have sufficiently high real part of the refractive index and small absorption (low imaginary part), yields the effect that is similar to metal covering layers while it also contributes to the enhancement of the evanescent waves. The concept of the enhancement of evanescent energy will hold for any combination of the considered substrate and cover layer (as given in Table 1), while the medium between the layered substrate and lens is either air, water or oil (the latter two for immersion applications), so that, together, it creates an asymmetric waveguide $n_2 > n_1$ and $n_2 > n_3$.

The introduction of the covering layer of large (compared to the wavelength) thickness is a no-go solution. If the covering layer is too thick, the original properties of the substrate might be debased. Conversely, thin films of approximately $\lambda/20$ which allow for guiding of at least one mode and consequently boost of the evanescent field, keep the design simple and compact [12].

Another important issue in the choice of materials is the deposition process. In Table 1, we include, for each material, the traditional deposition processes. The fabrication accuracy and the temperature requirement vary. So, for instance, CVD processes run at much higher temperatures than PVD processes (usually between 300°C and 900°C) which can be inappropriate to cover glass or plastic substrates directly because they cannot tolerate such temperatures. Also, PVD has a distinct advantage because it has a more precise film thickness control, in the order of sub-nm precision. This is important in our application, considering the required thickness of the thin film (around 10-20 nm).

4. Numerical results

For the simulations, we performed both 1D multilayer method [13] to analyse the Fresnel reflection coefficients when the substrate plus layer system is excited by evanescent waves, and rigorous 3D vectorial simulations using a homemade finite element method [14] to analyse the scattering enhancement due to a the presence of a particle on the top of the substrate plus layer system. In both 1D and 3D problems, the substrate roughness is neglected. The 1D simulations give insight to understand the background that would be created if either *s*- or *p*-polarized plane wave is incident at the interface in the absence of a scattering object. This step is necessary to determine the thickness that maximizes the evanescent components at the interface where the particle will lie. It is also important to look at both polarization components, *s* and *p*, because the incident field will include them both, for example, a tightly focused linearly polarized beam. The complex refractive index $\underline{n} = n + i * k$ for thin film of varying thickness that accounts for small changes in absorption is simulated through the software package OpenFilters [15]. The simulations are done for the wavelength of 405 nm, and the numerical aperture of the system (for the 3D simulations) was equal to $NA = 0.9$.

Correspondingly to the 3-layer system introduced in the Fig. 1(B) we show the cavity in Fig. 2(A). We consider a middle layer whose index of refraction is n_2 and thickness is d_2 surrounded by an input medium of index n_1 and an output medium with n_3. An incoming wave is from the left with an incident wavevector $\overrightarrow{k_1} = 2\pi/\lambda * n_1 \overrightarrow{u}$, where $\overrightarrow{u}$ is a unit vector. We assume the plane wave incidence where total vector $\overrightarrow{k_1} = \overrightarrow{k_{z1}} + \overrightarrow{k_x}$ consists of the normal $\overrightarrow{k_{z1}}$ and longitudinal $\overrightarrow{k_x}$ wavevector component. The wave incoming onto the slab is partially reflected and partially transmitted through the layer. The transmitted part reaches subsequently the second interface and will either be reflected or transmitted again. According to the literature [13] and [16] by adding all the coherent amplitudes for reflection or for transmission we arrive at the equations known as Fabry-Perot (FP) formulas for a single cavity which are exact, valid for the

OSA CONTINUUM

input of evanescent waves, work with any thickness of d_2. Here we only use the reflected part:

$$r = r_{12} + \frac{t_{12}t_{23}r_{23}exp(ik_{z2}d_2)}{1 - r_{23}r_{21}exp(i2k_{z2}d_2)} \tag{1}$$

where $k_{z2} = \sqrt{k_0^2 n_2^2 - k_x^2}$ is the z component of the wavevector in the medium 2, the Fresnel reflection and transmission coefficients at each interface $t_{12}, t_{23}, r_{23}, r_{21}$ are shown in the Fig. 2(A), and the refractive index n, which can be complex valued.

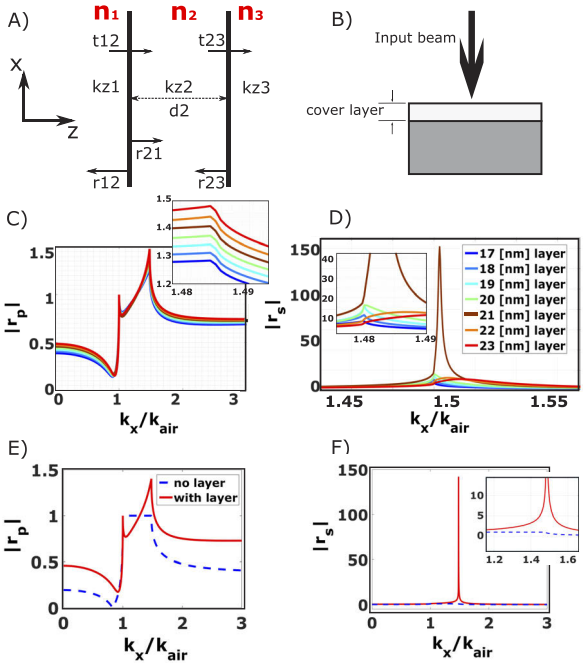

Fig. 2. Incident reflected and transmitted waves for three media layered structure A). Scheme of the simulation system B). Fresnel reflection coefficients for the three layer medium (air as input medium, TiO_2 as thin layer and glass as substrate). C) and D): absolute value of the Fresnel reflection coefficients as a function of the thickness of the TiO_2 layer for p and s polarizations, respectively, when the thickness of the covering layer changes from 17 to 23 nm. For the case of 21 nm thick TiO_2 layer, we show in E) and F) the Fresnel reflection coefficients with (red) and without (blue) the thin layer.

The notation can be generalized to r_{nm} (t_{nm}) with n and $m \in 1$, 2 or 3 being the reflection (transmission) coefficient corresponding to the wave reaching the interface from one medium n to another m. Hence, for specific s or p polarization of light, the Fresnel coefficients are computed by the following relations in wave vectors notation.

$$r_{nm}^{(s)} = \frac{\mu_m k_{zn} - \mu_n k_{zm}}{\mu_m k_{zn} + \mu_n k_{zm}}, r_{nm}^{(p)} = \frac{\epsilon_m k_{zn} - \epsilon_n k_{zm}}{\epsilon_m k_{zn} + \epsilon_n k_{zm}} \tag{2}$$

$$t_{nm}^{(s)} = \frac{2\mu_m k_{zn}}{\mu_m k_{zn} + \mu_n k_{zm}}, t_{nm}^{(p)} = \frac{2\epsilon_m k_{zn}}{\epsilon_m k_{zn} + \epsilon_n k_{zm}} \tag{3}$$

where ϵ is the material's relative permittivity, and μ is its relative permeability both set to 1. One notices that a particular combination of $k_x > k_0 n$ will render the imaginary value for k_z that represents an evanescent wave. Since we are interested in maximizing the evanescent wave in

OSA CONTINUUM

the reflection mode next to the particle, i.e. in the medium of air with $n_1 = 1$, we will study the reflection as the function of in-plane wavevector not only for the propagating modes $k_x < k_0 n_1$ but also higher spatial frequencies $k_x > k_0 n_1$. Further in the paper $k_0 n_1 = k_{air}$.

Here we show simulations for TiO_2 as a thin layer on glass; the same procedure was used for the Ta_2O_5. For Ta_2O_5, the Sellmeir equation [17] Eq. (4) is used to approximate the real part of refractive index of the weakly absorbing thin film:

$$n^2(\lambda) = 1 + \frac{B_1\lambda^2}{\lambda^2 - C_1} + \frac{B_2\lambda^2}{\lambda^2 - C_2} + \frac{B_3\lambda^2}{\lambda^2 - C_3}$$
$$B_1 = 3.3,\ C_1 = 0.005$$
$$B_2 = 0.2,\ C_2 = 0.01 \tag{4}$$
$$B_3 = 0.1,\ C_3 = 0.02$$

and the Cauchy equation [18] Eq. (5) is used for the TiO_2 film:

$$n(\lambda) = B + \frac{C}{\lambda^2}$$
$$B = 0.025614,\ C = 0.0059846 \tag{5}$$

The choice for this configuration is obtained by selecting the system with the strongest contribution of the evanescent waves.

For a three layer system (air-thin layer-glass, see scheme in subfigure 2(B), we plot in subfigures C) and D) of Fig. 2 the Fresnel reflection coefficients of s and p input polarization for layer thicknesses ranging from 17 to 23 nanometers for the case of TiO_2 as thin layer. In subfigures E) and F) we show the comparison between the absolute value of the Fresnel reflection coefficients for the bare (no thin layer) and covered substrate with 21 nm of TiO_2. Specifically, the region of spatial frequencies $k_x/k_{air} > 1$ is interesting because it represents the non-propagating waves, where for values of r_p and $r_s > 1$, it means amplification. It is evident that the presence of a thin layer such as TiO_2 results in a growth of the evanescent field. Moreover, the region of spatial frequencies $k_x/k_{air} < 1$ is also higher with the layer than without, but not as much as the evanescent part. This effect is expected because the contrast between air and TiO_2 is higher than contrast between air and glass $n_{TiO2} > n_{glass} > n_{air}$.

Once the thickness of the layer is selected, we consider the glass substrate with 21 nm of TiO_2 for the full 3D configuration to evaluate the effects of the polarization states of the probing focused light with and without the particle on it. This leads us to perform 3D rigorous simulation with the incident light focused at the top layer, and including a nanoparticle at the center of the focused beam (see Fig. 3(B)). The field components as part of the illumination cone interacts with both particle and substrate. The diameters of the polystyrene (PSL) nanoparticles are either 50 or 40 nm. When the beam is focused, all incident angles and polarisation components within the numerical aperture of the objective should be considered.

We calculate the scattered near and the far-field maps of the particle on top of the bare and covered with thin layer substrate illuminated by the focused laser beam. Scattered field computed by subtracting the portion that is caused by the given incident field when only the multilayer is present from the total field in the presence of the particle. With different polarization states, two of them are conventionally polarized laser beams such as linear and circular, while the other two are cylindrically polarized beams, namely radial and azimuthal (for linear and radial polarization see Fig. 3(A)). The boost in the near (all planes) and far field is evident and present in all four cases. The total near field in XZ plane for the case of linear polarization along x-axis is shown in Fig. 3(B) and the far field maps that for linear and radial polarization in Fig. 3(C) and (D). The far field is obtained over spatial frequency/angle within the numerical aperture of the system; this distribution corresponds to the pattern that falls onto the split detector. The color-code is such that

OSA CONTINUUM

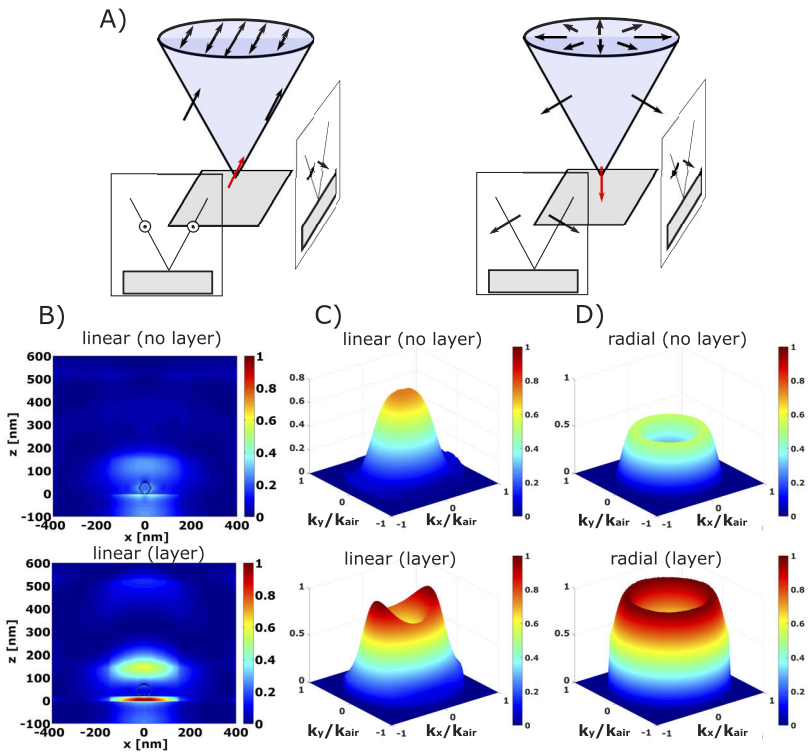

Fig. 3. A) Schematic drawing showing linearly (left) and radially (right) polarized light being focused on the substrate, with the electric field in focus at the optical axis shown in red. B) The near field distribution when linearly, along the x-axis polarized light is focused onto a 50 nm PSL nanoparticle on top of the substrate, without (top) and with (bottom) enhancement layer. C) and D) The far field-maps without (top) and with (bottom) layer for the case of linear polarization and radial polarization, respectively. The enhancement layer is 21 nm of TiO_2, the wavelength is 405 nm and numerical aperture is NA = 0.9. The color-code is such that the observed intensity is normalized by the maximum value of the far-field when the TiO_2 layer is present.

the observed intensity is normalized by the maximum value of the far-field when the TiO_2 layer is present. Following the near-field enhancement as in Fig. 3(B), we observe that linear polarization causes the far field to grow and remarkably change its angular distribution in 3(C). In the case of radial polarization, the far field is also enhanced but does not considerably change in shape (3(D)). The central part of the far field map is suppressed and it is biggest in the region where spatial frequencies exceed approximately $k_x/k_{air} > 0.2$, corresponding to acceptance angles higher than 11.5° with respect to the normal. The angular distribution of the far-field can be firstly explained by the shape of the focused spot in the focal plane. The x linearly polarized beam, left 3(A), has the focal spot elongated along the polarization axis, leading to the far field map that is also a bit wider in the x direction rather than y, with no rotational symmetry. For the focusing of radially polarized light, (3(A), right side), we understand that the strong longitudinal component of the electric field at the optical axis is responsible for the hollow central part of the far-field map and the rotational symmetry of the spot also translates to the far-field. Secondly, due to the sole *p* or joint *s* and *p* polarization content of the radially and linearly polarized beams, respectively, after the scattering from the particle on the enhancement layer, (3(C) and (D), bottom), the propagating

OSA CONTINUUM

and evanescent-converted components lead to destructive or constructive interference in different parts of the optical pupil.

Next, to quantitatively evaluate the enhancement that each polarization produces, we introduce the far-field gain factor G. In the equations below Eqs. (6–8) , we look at two metrics: G_{int} and G_{max}. These metrics represent the ratio between covered and bare substrate regarding the total scattered far-field intensity. To obtain G_{int}, we integrate the total far-field, while G_{max} relies on the maximum value of corresponding total field distribution:

$$G_{int} = \frac{I_{Cov\_int}}{I_{Bare\_int}} \qquad I = \int_{n=1}^{nrows} \int_{m=1}^{ncol} I(n,m)dndm \tag{6}$$

$$G_{max} = \frac{I_{Cov\_max}}{I_{Bare\_max}} \qquad I_{max} = max(I(n,m)) \tag{7}$$

$$I(n,m) = (|E_x(n,m)|^2 + |E_y(n,m)|^2) \tag{8}$$

The integrals above are calculated by the trapezoidal method. Despite the metric that we use, either integral or based on maximum value, the gain factor expected by the cyllindrically polarized light is superior to conventionally polarized beams, as shown in Table 2.

Table 2. The gain factors indicate that cylindrically polarized light produces higher gain in the far-field as compared to the conventional polarizations. The material TiO_2 shows better performance than Ta_2O_5. The maximum gain in each column is given in bold. The diameter of particle is 50 nm.

Polarization	G_{max}		G_{int}	
state	Ta2O5	TiO2	Ta2O5	TiO2
Linearly X	1.13	1.32	1.65	1.97
Radially	2.04	**2.91**	**2.49**	**3.76**
Azimuthally	**2.08**	2.86	2.47	3.53
Cicularly	1.04	1.13	1.65	1.97

By observing the far-field angular distribution for various polarizations, one conclude that for both linear and circular polarization, the central part of the far field is almost not enhanced as compared to the enhancement at the edges of the pupil, whereas in the case of azimuthal and radial polarization, the enhancement occurs to all angles. However, for all polarisations, the position of the maxima of the distribution lies in the high angular range $k_x/k_{air} > 0.2$. This is the one additional reason why we have introduced the G_{max} factor. For example, the G_{max} parameter for the TiO_2 layer and particle of 50 nm is equal to 2.91 for radial polarisation. This suggests that applying an annular aperture at the detector plane can yield better sensitivity. In fact, the benefit of the detection with annular aperture was demonstrated in previous research [19]. In that reference, it was anticipated that the collected far field at higher angles of the aperture are more influenced by the presence of the particle, and has been confirmed here with the far field simulations.

As can be seen from Table 2, we also introduce Ta_2O_5 material as enhancing layer, which has just slightly lower refractive index n and about the same level of absorption k as compared to TiO_2. Along the same procedure of defining the suitable thickness as introduced earlier, we consider a cover layer of 20 nm of Ta_2O_5. Due to slightly higher absorption, the evanescent amplification that surrounds the particle is lower so both G_{max} and G_{int} are inferior as compared to TiO_2.

OSA CONTINUUM

Further, to understand whether the evanescent wave conversion mechanism may explain the superior detection performance, we have studied how the value of the real and imaginary parts of the index of refraction of the enhancement layer influences the far-field increase. In order to do that, we perform a parametric sweep. A radially polarized beam focused at the center of the particle of diameter 30 nm, $NA = 0.9$ and enhancement layer with fixed thickness of 21 nm of a fictitious material is considered. We show in Fig. 4 the response of the far field as the values of the real or imaginary part of the refractive index varies. One parametric sweep is shown in Fig. 4(B) the imaginary part of refractive index remains fixed as $k = 0.133$ and n changes from 2.6 to 4 in 15 steps. Another sweep is shown in Fig. 4(C), where the real part of the refractive index remains fixed to $n = 2.66$ and k changes from 0.004 to 1.5 in 15 steps. Note, for the far-field cross-sections (4(D) and (E)) (radial polarization and particle is aligned with a spot), the scattered field is cyllindrically symmetric (as in 3(D)). The cross-section curves D) and E) are normalized to unity by the maximum value of the far field intensity from the corresponding parametric sweeps. For instance when $\underline{n} = 4 + i * 0.133$, that corresponds to the rightmost value in the parametric sweep B), the far-field cross-section (bottom of Fig. 4(D)) has the maximum value of 1 thus the enhancement is the highest

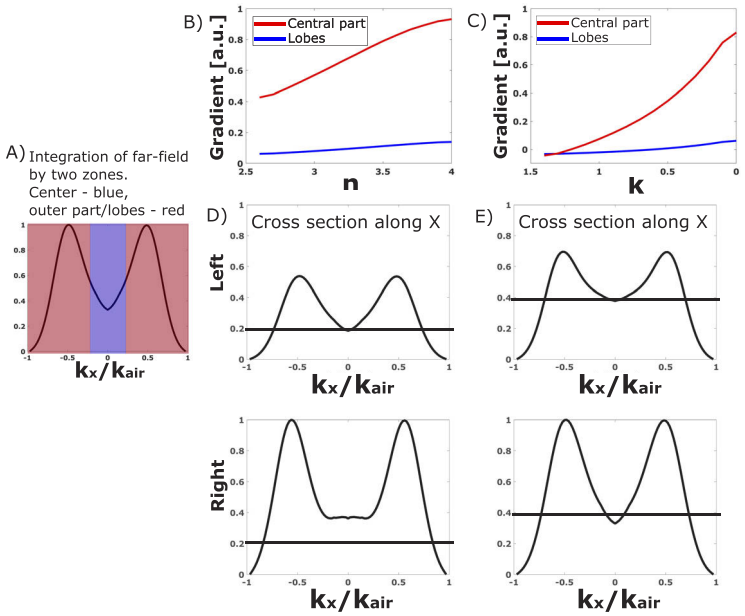

Fig. 4. A) Cross-section of the far field intensity along the x-axis when input beam is radially polarized and focused on a 30 nm nanoparticle. The middle zone in blue corresponds to the center of the pupil $|k_x/k_{air}| \leq 0.2$ and the surrounding hollow cone in red corresponds to $0.2 < |k_x/k_{air}| < 0.9$. B) Point per point gradient of the integrated electric field intensity of the blue and red regions of the far field as a function of the real index of refraction with the imaginary part kept at the value of 0.133, C) as function of the imaginary part of the index of refraction with the real part kept at the value of 2.6. D) and E) profile of the field distributions corresponding to the left- and right-most values of the refractive indexes of plots B) and C), respectively. Black lines mark the centre of the cross-section $k_x/k_{air} = 0$ that corresponds to the beginning of refractive indexes sweep.

In order to emphasize the region of the pupil where either propagating or converted-evanescent components contributes, we integrate the total field by two zones: $|k_x/k_{air}| \leq 0.2$ and $0.2 < |k_x/k_{air}| < 0.9$, seen as blue and red colour of the cross section in Fig. 4(A). The integral

OSA CONTINUUM

for total field intensity of both zones is calculated by applying the trapezoidal rule and on top of that we compute the gradient. From the profiles B) and C), one can see that the amount of energy that scatters to the outer parts of a pupil is greatly boosted when absorption is low (as it can be seen in the region where $k \leq 0.5$). Whereas upon increase of the real part of a refractive index ($n \geq 2.6$) the central and side contributions raise almost linearly. The index of refraction properties are varied separately because they have a major influence on either the propagating modes or the evanescent-converted components. Also, in Fig. 4(B), the growing behavior of the gradient can be characterized by an almost linear behavior of the total field in both central (blue curve) and outer part of the pupil (red curve). In contrast, if the absorption decreases from $k = 1.5$ to $k = 0.133$ (see Fig. 4(E) top and bottom, respectively), the level of the field in the center of the pupil remains almost constant while the slope grows more rapidly at the lobes in lowest absorption value. In other words, allowing for the absorption to be as low as possible is the key mechanism to increase the ratio between the scattering at the higher angles as compared to the lower ones. This behavior seems to be achieved mainly by the evanescent components at the interface converted to propagating modes by the presence of the isolated particle on top of the covering layer. The topographical contrast of optical detection is of significant interest for techniques that rely on differential detection principle, such as the one we propose. Equally important, by considering materials with large real part of refractive index, one can achieve large enhancements of the full far-field distribution. That is important for applications that benefit from low power of illumination.

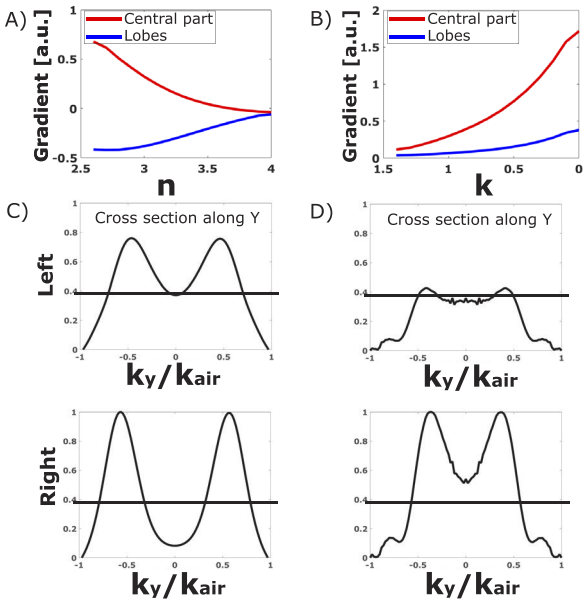

Fig. 5. Point per point gradient of integrated electric field intensity as function of the real and imaginary parts of the refractive index for the case of linear polarization along the X direction when A) the real part value changes from 2.6 to 4 while the imaginary remains fixed at 0.133, and B) when the real part remains fixed at 2.66 while the imaginary part changes from 0.0004 to 1.4. C) and D) cross-sections of the total far-field pattern corresponding to the maximum and minimum values of the refractive indices of plots A) and B), respectively. The curves are normalized to unity by the maximum value of the distribution belonging to the particular parameter sweep. Black lines mark the centre of the cross-section $k_x/k_{air} = 0$ that corresponds to the beginning of refractive indexes sweep.

OSA CONTINUUM

Finally, we point out that the gradient profiles for the azimuthally polarized light are very close to those of the radially polarized ones. The major differences in directional tendency are observed in the sweep of the real value of the refractive index for both linear and circular polarization.

Similar to Fig. 4, we calculate the gradient of the integrated total field by two zones, central and outer part of the pupil for linear polarization as shown in Fig. 5. Compared to radial polarization, in case of linear polarisation, the gradient of integrated electric field intensity for both the real and imaginary parts of the refractive index is different. Also, because of the absence of rotational symmetry, we show in Fig. 5(C) and (D) the profiles in Y direction. For minimum (top) and maximum (bottom) value of n in C), and maximum (top) and minimum (bottom) k value in D). From the gradients in Fig. 5(B), one can see that the behavior is such that the energy grows faster towards the lobes and slower towards the center. But in 5(A), when $n \geq 3.2$, it levels out. This can be attributed to the fact that linear polarization has a mixture of s and p components in focus. Similar behavior is observed for circular polarization.

We have also studied the robustness of the enhancement process for variations on the thickness of the single layer. This is important parameter that should be taken into account since, experimentally, it is almost unavoidable that the actual thickness will vary as compared to the nominal one. The results of this analysis highlight the advantage of the evanescent wave-amplification method in terms of robustness. In Fig. 6, the behaviour of the total scattered far-field intensity as the function of the covering layer thickness is shown (integration over full pupil according to the trapezoidal method.)

The cover layer material in this case is TiO_2, having a constant refractive index of $n = 2.6632$, $k = 0.00423$ over the range of covering layer thickness from 0 to 200 nm. The size of the nanoparticle is 30 nm in diameter with the refractive index of $n = 1.58$ for the wavelength of illumination of 405 nm. From these plots, one can see that the deviation around the maximum of scattering for linear and radial polarization is about 0.84% and 0.71% per nm, meaning that the system is robust for a few nm thickness variations.

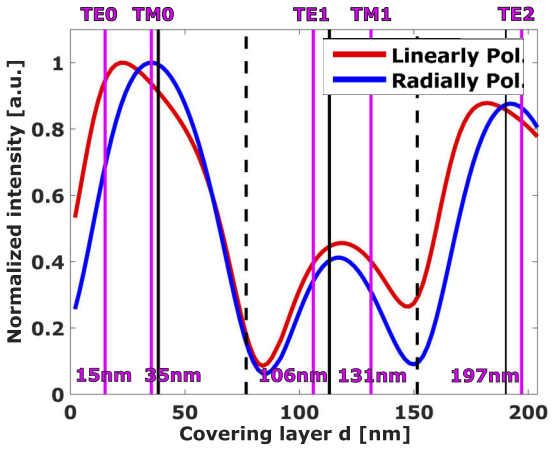

Fig. 6. The total scattered far-field intensity integrated over the pupil and normalized to unity for linearly polarized (red) and radially polarised light (blue). The positions of the guided modes of the three-layer 1-D slab are indicated in purple, and the positions of maxima and minima in reflection for the normally incident light in black solid and dashed lines correspondingly.

The same Fig. 6 can be used to show the influence of the thickness of the thin layer as it becomes much larger than the values we have considered so far. The maxima and minima fluctuations suggest that it could come from the excitation of modes on the 1D cavity that is

OSA CONTINUUM

formed of the 3-layer system without the presence of the particle. To illustrate that, we calculated the modes of this 3-layer system. In the vertical lines found in Fig. 6, we show the positions of the *TE* modes and *TM* modes (in purple). We pick positions of truly guided modes, whose spatial frequency k_x/k_{air} is comprised between the two highest indices inherent to the 3-layer structure. The positions of the first two modes, namely TE_0 and TM_0, supported in the waveguide are in good correspondence with the maxima of the far-field scattering for linearly and radially polarized light, respectively. Also, the positions of the minima of the reflected field of the 3-layer stack are in good agreement with the dips of the far-field scattering profile (black dashed lines of Fig. 6). A minimum in reflection affects mainly the secondary-scattered portion (from particle to substrate and further to the detector). Also, we can consider that the evanescent part of the guided modes for the thickness of the layer sufficiently larger than the cut-off of the particular mode after being re-scattered by the particle is not transferred to the far field at the angles of the acceptance cone. It becomes clear that for the particular design of the enhancing layer, maximum of scattering can be achieved when the layer supports just one mode that does correspond to the spectrum of excitation. Further increasing the thickness of the layer can have a drawback of falling into the local minima of reflectance, having dissipation, or having destructive interference upon interaction with particle due to the multiple modes of the waveguide. This simulation allows us to support the idea that the enhancement in scattering is due to the evanescent wave amplification, which becomes possible in the scenario when the probing light excites the dipolar-like response of the sphere at an interface. When exciting with linearly or radially polarized light, the dipolar-like response of mainly horizontal or vertical orientation will be excited and coupled to the structure of the waveguide beneath. Coupling is only possible if the radiation of dipole matches with the mode supported by the waveguide. If the requirement is fulfilled, modes will propagate in a slab and the evanescent part of the field is maximized, and so it can be re-scattered to the far field by the particle.

Finally, we point out that the shape of the far-field distribution is wavelength dependent, and also the size of the particle influences the angles of the scattering. Therefore, the result cannot be generalized for other wavelength regimes and particle sizes. However, for particles in the regime of $\lambda/9$ and all the states of polarization, the boost related to the evanescent amplification occurs.

5. Experimental results

From the experimental point of view, the enhancement present in the far field estimated numerically in the previous section can be demonstrated by comparing the scattered enhancement in a relative scale, i.e., by performing the same experiment with covered and uncovered substrates with the same nanoparticle material and size. However, only producing higher scattering does not give information on whether the gain is sufficient to overcome the background noise or not. Thus, it is difficult to predict the ultimate limit of this technique. In any case, in order to verify the validity of the calculations, we carried out several experiments. We use the setup earlier introduced and explained in Fig. 1. In Table 3, the fabricated samples are shown.

Table 3. Summary of the fabricated samples. The thickness of the layers has been measured with an ellipsometer.

Sample #	Design
1	glass + 40 nm spheres
2	glass + 50 nm spheres
3	glass + 20.3 nm Ta2O5 + 50 nm spheres
4	glass + 20.3 nm Ta2O5 + 40 nm spheres
5	glass + 22 nm TiO2 + 40 nm spheres

OSA CONTINUUM

For each sample, we find an isolated nanoparticle of the nominal size and then collect the far field maps for different polarization states such as linear, radial and azimuthal (Fig. 7). Each far field map is the result of averaging two repeated scans. As the detection is done using heterodyne technique [20], we modulate our diode laser with a square waveform of either V_{pp} = 1.7 V or V_{pp} = 1.8 V , so that the power on the substrate is either P_{low} = 0.02 mW or P_{high} = 0.026 mW, respectively. The higher power is used for the detection of 40 nm spheres. In order to compare the SNR with and without the thin layer, we define SNR gain G (in dB units) as Eq. (9):

$$G = \mathrm{SNR}_{(\mathrm{layer})} - \mathrm{SNR}_{(\mathrm{no\ layer})}, \text{ with } \mathrm{SNR}_{(.)} = 10\log_{10}\left(\frac{\mathrm{S}_{(.)}}{\mathrm{N}_{(.)}}\right) \tag{9}$$

The SNR is computed based on the profile with the highest amplitude, which corresponds to a probing beam scan across the centre of the spherical particle. Table 4 summarizes the measured gain enabled by the cover layer for different polarizations. All tested cases show that the enhancing layers do improve the detection of the low refractive index nanoparticles. The gain results are consistent with the simulations done previously that predicted that TiO_2 is a better material to enable evanescent wave amplification.

Table 4. SNR gain G [dB] due to evanescent wave amplification for the cases of detection of 50 and 40 nm particles on top of Ta_2O_5 or TiO_2 layers on glass (compared to glass with no layer), for various polarization configurations.

	SNR gain G [dB]		
Polarization State	d = 50 [nm]	d = 40 [nm]	d = 40 [nm]
	Ta2O5	TiO2	Ta2O5
Linearly X	7	11.8	11.5
Radially	5	9.3	6
Azimuthally	2.8	11.1	6.5

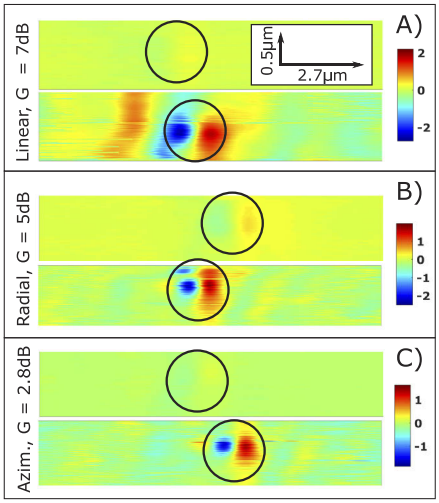

Fig. 7. The raw far-field signal maps of the glass sample without and with the enhancement layer of Ta2O5. Isolated PSL particle of 50 nm and linear A), radial B), azimuthal C) input polariziation of the beam. Each map is $2.7\mu m \times 0.5\mu m$.

There is an evident relationship between the size of the particle and the gain that is achieved with the layer. The smaller particles become visible, compared to the very low signal in the

OSA CONTINUUM

absence of the layer, while the bigger particles have already a SNR > 18 [dB] even without the layer. One reason for that is because the scattering cross-section is larger for 50 nm particles than for 40 nm. Below, we demonstrate the measured far-field signal maps, without/with layer of Ta_2O_5 (samples number 2 and 3) for the case of d = 50 nm PSL particle and three input polarizations as according to the first column of 4.

The results show that the cylindrically polarized beams can contribute to a relatively big gain (G of 9.3 [dB] or 11.1 [dB]), yet, it is important to highlight that we have observed experimentally that the use of linearly polarized light is superior to cylindrically polarized light. In Fig. 8 we show the results for sample number 5. Even though the particle of 40 nm diameter is visible when radially or azimuthally polarized beams are used (Fig. 8(B) and (C)), one can clearly see that for the linearly polarized light, the signal is much stronger (Fig. 8(A)).

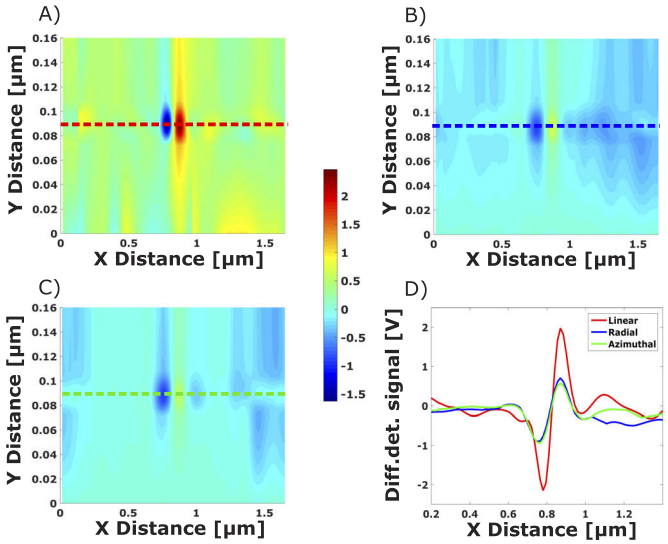

Fig. 8. Split detector signal as a function of the relative position of the particle w.r.t. the focused field as the particle is scanned in the X direction. The particle is on a glass sample with the enhancement layer of TiO_2 and 40 nm PSL with the linear A), radial B), and azimuthal C) polarization of the probing beam. The colour scheme scales to the limits of the linearly polarized beam. The cross-section of the corresponding signals are compared in panel D).

6. Discussion

In this work, the wavelength of the probing light was chosen in accordance with our experimental settings, but in general, this parameter can also be optimized together with the others. The study of resonant wavelength combined with evanescent wave amplification can extend the application of this technique to a wide range of applications. As predicted, our experiments demonstrate gain in the far-field due to the re-scattered evanescent field generated from the particle at a layered structure. Contrary to expectations, we did not find a significant benefit of changing the polarization of the probe to cylindrically polarization. We observed lower SNR as compared to linear polarisation, even in the case of no thin layer on top of the substrate. A possible explanation could be the complexity of the experiment. Producing and focussing radial/azimuthal polarisation is more difficult than linear polarisation. For instance, with radially polarized light, the alignment of the beam w.r.t. the objective as well as the quality of the radial (azimuthal) polarization are very critical in order to obtain a very tight symmetrical focused spot.

OSA CONTINUUM

7. Conclusion

In this paper, we studied the enhanced far-field scattering of single spherical PSL particles deposited on top of a glass substrate covered with a thin layer of dielectric material. The key to the far-field enhancement effect is to achieve first substantial field enhancement in the near-field. By simply looking at the interface between the air and the top surface of the bare/covered substrate, we concentrate our attention on maximizing the region of spatial frequencies that corresponds to the enhancement of evanescent waves. The ultimate sensitivity of the detection is limited by both propagating components that interact with the particle and also by the amount of evanescent waves that are converted to propagating waves.

From the research that has been conducted, a gain factor greater than one has been experimentally observed for different polarizations (linear, radial, azimuthal). Furthermore, in the experiment, the use of linearly polarized light has shown superior performance for the detection of 40-50 nm nanoparticles. To understand the mechanism of the evanescent wave amplification, our analysis show that both values of n and k of the material are important, with large real part of the refractive index and low absorption being the key elements. This technique is robust to the deviations of the thickness of the cover layer. For the particular design of the enhancing layer, the maximum of scattering is achieved when the layer supports just one mode that does correspond to the spectrum of excitation. Further increasing the thickness of the layer can have a drawback of falling into local minima of reflectance from where the observed scattered field will become smaller. Due to the directionality of the scattering from the nanoparticle, applying an annular aperture at the detector can be beneficial.

The proposed technique can be successfully used in applications such as bio-nano detection and contamination detection in the semiconductor or flexible electronics industry. For instance, materials such as Si_3N_4 silicon nitride ($n \approx 2$ and almost zero absorption at 405 nm) can serve the dual purpose because they are inherently present as a top layer of poly-silicon pellicle [21] or in PET plastic substrates [22]. Furthermore, there is a potential for this technique to be implemented in interference reflectances imaging techniques such as IRIS and iSCAT. In these label-free techniques, the excellent smoothness and flatness of the substrate are crucial [3]. Finally, one can also mention spinning bio disks for lab-on-chip devices, where the dipolar-like scattering of the particle near the surface is required to be maximized [23].

Funding

Nederlandse Organisatie voor Wetenschappelijk Onderzoek (14660, Applied and Technical Sciences division (TTW), High Tech Systems and Materials Research Program).

Acknowledgments

We gratefully acknowledge the help provided by TNO in the fabrication of samples. Dmytro Kolenov acknowledges the High Tech Systems and Materials Research Program with Project n. 14660, financed by the Netherlands Organisation for Scientific Research (NWO), Applied and Technical Sciences division (TTW) for funding this research.

Disclosures

The authors declare no conflicts of interest.

References

1. J. Su, A. F. G. Goldberg, and B. Stoltz, "Label-free detection of single nanoparticles and biological molecules using microtoroid optical resonators," Light: Sci. Appl. **5**(1), e16001 (2016).
2. A. Salehi-Reyhani, "Evaluating single molecule detection methods for microarrays with high dynamic range for quantitative single cell analysis," Sci. Rep. **7**(1), 17957 (2017).

OSA CONTINUUM

3. F. Ekiz-Kanik, D. D. Sevenler, N. L. Ünlü, M. Chiari, and M. S. Ünlü, "Surface chemistry and morphology in single particle optical imaging," Nanophotonics **6**(4), 713–730 (2017).
4. D. Sevenler, O. Avci, and M. S. Ünlü, "Quantitative interferometric reflectance imaging for the detection and measurement of biological nanoparticles," Biomed. Opt. Express **8**(6), 2976–2989 (2017).
5. S. Nie and R. N. Zare, "Optical detection of single molecules," Annu. Rev. Biophys. Biomol. Struct. **26**(1), 567–596 (1997).
6. O. Avci, C. Yurdakul, and M. S. Ünlü, "Nanoparticle classification in wide-field interferometric microscopy by supervised learning from model," Appl. Opt. **56**(15), 4238–4242 (2017).
7. O. Avci, M. I. Campana, C. Yurdakul, and M. S. Ünlü, "Pupil function engineering for enhanced nanoparticle visibility in wide-field interferometric microscopy," Optica **4**(2), 247–254 (2017).
8. S. Roy, S. F. Pereira, H. P. Urbach, X. Wei, and O. El Gawhary, "Exploiting evanescent-wave amplification for subwavelength low-contrast particle detection," Phys. Rev. A **96**(1), 013814 (2017).
9. O. E. Gawhary, N. J. Schilder, A. da Costa Assafrao, S. F. Pereira, and H. P. Urbach, "Restoration of s-polarized evanescent waves and subwavelength imaging by a single dielectric slab," New J. Phys. **14**(5), 053025 (2012).
10. P. Bussink, J.-B. Volatier, P. van der Walle, E. Fritz, and J. van der Donck, "Sub 20nm particle inspection on euv mask blanks," Proc. SPIE **9778**, 977835 (2016).
11. Y. Lu and S. C. Chen, "Nanopatterning of a silicon surface by near-field enhanced laser irradiation," Nanotechnology **14**(5), 505–508 (2003).
12. D. G. S. Zhiyong Ma, *Metrology and Diagnostic Techniques for Nanoelectronics* (Pan Stanford, 2016).
13. O. E. Gawhary, M. C. Dheur, S. F. Pereira, and J. J. M. Braat, "Extension of the classical fabry–perot formula to 1d multilayered structures," Appl. Phys. B **111**(4), 637–645 (2013).
14. X. Wei, A. J. Wachters, and H. P. Urbach, "Finite-element model for three-dimensional optical scattering problems," J. Opt. Soc. Am. A **24**(3), 866–881 (2007).
15. S. Larouche and L. Martinu, "Openfilters: open-source software for the design, optimization, and synthesis of optical filters," Appl. Opt. **47**(13), C219–C230 (2008).
16. M. Born, E. Wolf, A. B. Bhatia, P. C. Clemmow, D. Gabor, A. R. Stokes, A. M. Taylor, P. A. Wayman, and W. L. Wilcock, *Principles of Optics: Electromagnetic Theory of Propagation, Interference and Diffraction of Light* (Cambridge University Press, 1999), 7th ed.
17. W. Sellmeier, "Ueber die durch die aetherschwingungen erregten mitschwingungen der körpertheilchen und deren rückwirkung auf die ersteren, besonders zur erklärung der dispersion und ihrer anomalien," Ann. Phys. **223**(11), 386–403 (1872).
18. J. W. Gooch, *Cauchy's Dispersion Formula* (Springer, 2011), pp. 125.
19. S. Roy, A. C. Assafrao, S. F. Pereira, and H. P. Urbach, "Coherent fourier scatterometry for detection of nanometer-sized particles on a planar substrate surface," Opt. Express **22**(11), 13250–13262 (2014).
20. D. Kolenov, R. C. Horsten, and S. F. Pereira, "Heterodyne detection system for nanoparticle detection using coherent Fourier scatterometry," in *Optical Measurement Systems for Industrial Inspection XI*, vol. 11056 P. Lehmann, W. Osten, and A. A. G. Jr., eds., International Society for Optics and Photonics (SPIE, 2019), pp.336–342.
21. D. Brouns, A. Bendiksen, P. Broman, E. Casimiri, P. Colsters, P. Delmastro, D. De Graaf, P. Janssen, M. van de Kerkhof, R. Kramer, M. Kruizinga, H. Kuntzel, F. van der Meulen, D. Ockwell, M. Peter, D. Smith, B. Verbrugge, D. van de Weg, J. Wiley, and P. van Zwol, "Nxe pellicle: offering a euv pellicle solution to the industry," Proc. SPIE **9776**, 97761Y (2016).
22. K. Kim, K. Kim, Y. Ji, J. Park, J. Shin, A. Ellingboe, and G. Yeom, "Silicon nitride deposition for flexible organic electronic devices by vhf (162 mhz)-pecvd using a multi-tile push-pull plasma source," Sci. Rep. **7**(1), 13585 (2017).
23. D. D. Nolte, "Invited review article: Review of centrifugal microfluidic and bio-optical disks," Rev. Sci. Instrum. **80**(10), 101101 (2009).